Electron-beam broadening in electron microscopy by solving the electron transport equation

Erich Müller[1,*] Milena Hugenschmidt[1,2] and Dagmar Gerthsen[1,2]

[1]*Laboratory for Electron Microscopy, Karlsruhe Institute of Technology (KIT), Engesserstr. 7, 76131 Karlsruhe, Germany*

[2]*3DMM2O - Cluster of Excellence (EXC-2082/1 – 390761711), Karlsruhe Institute of Technology (KIT), 76131 Karlsruhe, Germany*

(Received 18 August 2020; accepted 28 October 2020; published 4 December 2020)

Scanning transmission electron microscopy (STEM) and scanning electron microscopy (SEM) are prominent techniques for the structural characterization of materials. STEM in particular provides high spatial resolution down to the sub-ångström range. The spatial resolution in STEM and SEM is ultimately limited by the electron-beam diameter provided by the microscope's electron optical system. However, the resolution is frequently degraded by the interaction between electron and matter leading to beam broadening, which depends on the thickness of the analyzed sample. Numerous models are available to calculate beam broadening. However, most of them neglect the energy loss of the electrons and large-angle scattering. These restrictions severely limit the applicability of the approaches for large sample thicknesses in STEM and SEM. In this work, we address beam broadening in a more general way. We numerically solve the electron transport equation without any simplifications, and take into account energy loss along the electron path. For this purpose, we developed the software package CeTE (Computation of electron Transport Equation). We determine beam broadening, energy deposition, and the interaction volume of the scattered electrons in homogeneous matter. The calculated spatial and angular distributions of electrons are not limited to forward scattering and small sample thicknesses. We focus on low electron energies of 30 keV and below, where beam broadening is particularly pronounced. These electron energies are typical for SEM and STEM in scanning electron microscopes.

DOI: 10.1103/PhysRevResearch.2.043313

I. INTRODUCTION

Scanning electron microscopy (SEM) and scanning transmission electron microscopy (STEM) are prominent techniques to study the structural properties of solids and soft matter materials. Spectacular results were obtained in the more recent past by STEM, which has revealed details of the atomic structure of materials [1–4]. This can be attributed to the success in correcting aberrations of electron lenses that has led to electron beam diameters distinctly below the sub-ångström range [5–7]. However, the spatial resolution of images and analytical techniques in electron microscopy does not only depend on the beam diameter provided by the microscope's condenser-lens system but is also strongly affected by the broadening of the electron beam while passing through matter. This is particularly relevant if the primary electron energy in transmission electron microscopes is lowered from standard values between 80 and 300 keV. The reduction of the electron energy came into focus in the more recent past, because knock-on damage can be avoided and contrast-to-noise-ratio of weakly scattering materials is enhanced [8,9]. With growing interest in low-energy electron microscopy, more attention is paid to the calculation and measurement of beam broadening [10–12]. The mean-free-path length of electrons decreases with the electron energy, yielding an increasing number of scattering events. This degrades STEM resolution because substantial beam broadening occurs already at small sample thicknesses. We note that beam broadening also limits STEM resolution for large sample thicknesses at standard electron energies of 80 keV and above [13].

Compared to STEM, SEM is an even more wide-spread technique in materials characterization. Electron energies of 30 keV and below are generally used to study the near-surface properties of bulk materials. The resolution in the 1-nm range is strongly influenced by the interaction volume, i.e., the volume in the sample where primary, secondary, and backscattered electrons are located. In SEM, the reduction of the electron energy to even lower values than 30 keV is favorable because the size of the interaction volume decreases. This is particularly relevant for SEM imaging with backscattered electrons (defined as electrons with energies between 50 eV and the primary electron energy), which is applied to obtain SEM images showing material contrast. The size and shape of the interaction volume in dependence of the primary electron energy were revealed by exposing a layer of positive electron resist to an electron beam [14]. However, the spreading of the primary electrons within a sample cannot be directly visualized and must be calculated.

Concerning electron-beam broadening in STEM, several analytical models were elaborated to calculate the electron-beam diameter at the exit plane of electron-transparent

*Corresponding author: erich.mueller@kit.edu

samples by considering differential scattering cross sections to describe multiple scattering [15,16]. Further early approaches describe beam broadening by assuming a Gaussian distribution of the electrons after passing through matter [17,18]. A more general model dealing with a wider range of collision numbers up to 25 has been proposed by Gauvin and Rudinsky [10]. All analytical approaches mentioned here require approximations to model the complex multiple scattering of electrons because large-angle scattering and energy loss are neglected. While the approaches above describe electron-transparent samples and neglect energy loss, the calculation of the electron range for bulk samples requires the consideration of energy loss. Reimer has summarized various definitions of the electron range and gave estimation formulas for the range-energy relation [18].

Monte Carlo simulations were established already decades ago and are well suited to calculate beam broadening in STEM and the size of the interaction volume in bulk samples in SEM [19]. More recent applications concern the calculation of beam broadening in STEM by, e.g., Gauvin and Rudinsky, Drees *et al.*, Hugenschmidt *et al.*, and de Jonge *et al.* [10–11]. Monte Carlo simulations generally can avoid restrictive simplifications. However, to obtain statistically relevant data, a large number of electron trajectories have to be simulated [19]. This can be time-consuming if simulations have to be performed for a large parameter range.

A more general way of treating electron scattering and beam broadening is based on the solution of the electron transport equation in the formulation of Goudsmit and Saunderson and of Lewis [20,21]. The Lewis formalism is more elaborate and accounts for energy loss by the slowing down of the electrons along the path length. It also yields analytical equations for the moments of the spatial electron distribution like the mean and variance of the electron displacement and scattering direction. First- and second-order moments can be determined in a generalized formulation by solving the electron transport equation [22]. Unlike the Monte Carlo formalism, the solution of the transport equation provides results without dividing the electron path into consecutive steps, which affects the computation, particularly at large path lengths. In addition, the direct solution of the transport equation is not subjected to statistical errors.

An attempt to solve the electron transport equation for multiple scattering was implemented by Rez to address beam broadening [23]. This approach is based on Fourier transformations of the transport equations but neglects large-angle scattering and energy loss.

We note that all the above-mentioned methods provide probability distributions for electrons by considering electrons as particles. Thus, the influence of electron channeling and diffraction effects on beam broadening cannot be taken into account by the models considered in this work. Electron channeling and diffraction are interference phenomena and require the treatment of electrons as waves as shown by Voyles *et al.* and Wu *et al.* [24,25]. These effects can be neglected for the discussion of beam spreading and of the interaction volume as soon as the ratio of coherent to incoherent scattering becomes small. Coherence prevails only for very thin specimens, where the sample thickness does not significantly exceed the mean-free path length for electron scattering.

Besides Monte Carlo calculations, all other descriptions for beam broadening discussed above neglect energy loss and high-angle scattering. In this work, we address beam broadening in STEM and SEM in a more general way. The electron transport equation in Lewis's formulation [21] is solved numerically without any simplifications and by considering energy loss and energy straggling along the electron path. Electron ranges are determined numerically by calculating the path length where the electrons completely lose their energy. The new approach of this work is to use the moments obtained from the solution of the transport equation [21,22,26] to determine beam broadening, energy deposition, and the interaction volume of the scattered electrons. The calculated spatial and angular electron distributions are not limited to forward scattering but apply also to electron backscattering. Beam broadening is studied by the method of moments (MM) for all scattering regimes, applicable both for electron-transparent samples and bulk materials where no electrons are transmitted. Representative results are shown for silicon, copper, and platinum, which differ significantly in atomic number and material density. We focus on low electron energies of 30 keV and below, which are typical for SEM and STEM in scanning electron microscopes.

II. METHODS

A. Basics of electron transport in matter

To determine the spatial and angular distribution of electrons after multiple scattering along a traveled path, the electron transport theory is considered in the exact formulation of Lewis [21] and its generalization given by Kawrakow and Bielajew [22]. Assuming that an electron impinges perpendicular on the sample surface in the direction of the z axis, the probability density f of finding the electron after traveling the path length s at the position $\boldsymbol{x}$ moving in direction $\boldsymbol{v}$ is denoted by $f(s,\boldsymbol{x},\boldsymbol{v})$. The electron transport process is described by

$$\frac{\partial f(s,\boldsymbol{x},\boldsymbol{v})}{ds} + \boldsymbol{v}\cdot\nabla f(s,\boldsymbol{x},\boldsymbol{v}) = N\int d\boldsymbol{v}'[f(s,\boldsymbol{x},\boldsymbol{v}') - f(s,\boldsymbol{x},\boldsymbol{v})]\sigma(|\boldsymbol{v}-\boldsymbol{v}'|), \quad (1)$$

where $\sigma(|\boldsymbol{v}-\boldsymbol{v}'|)$ denotes the differential scattering cross section per unit scattering angle $d\Omega$, corresponding to the deflection $\boldsymbol{v}' \rightarrow \boldsymbol{v}$. N is the number of atoms per unit volume.

By expanding $f(s,\boldsymbol{x},\boldsymbol{v})$ in spherical harmonics, Lewis obtained general expressions for the angular distribution and the moments of the spatial distribution [21]. The angular distribution after a path length s is given by

$$F(\theta,s) = \int f(s,\boldsymbol{x},\boldsymbol{v})\,d\mathbf{x} = \sum_{l=0}^{\infty}\frac{2l+1}{4\pi}\exp(-sQ_l)\,P_l(\cos\theta) \quad (2)$$

and corresponds to the result found also by Goudsmit and Saunderson [20].

P_l are the Legendre polynomials and Q_l is the l th transport coefficient given by

$$Q_l = \frac{2\pi}{\lambda}\int_{-1}^{1}[1-P_l(\cos\theta)]f_1(\cos\theta)d(\cos\theta), \quad (3)$$

with the single scattering function

$$f_1(\cos\theta) = \frac{1}{\sigma}\frac{d\sigma(\cos\theta)}{d\Omega}. \tag{4}$$

Here λ denotes the mean-free path length given by $\lambda = 1/(N\sigma)$, where σ is the total (elastic and inelastic) scattering cross section. The solid angle is given by $d\Omega$.

The Lewis approach accounts additionally for the energy loss of the multiple-scattered electrons using a slowing-down approximation. The transport coefficients from Eq. (3) are considered as energy-dependent and connect the energy loss of the electrons with the traveled path length s. They are rewritten as G_l:

$$G_l = \int_0^s Q_l(s')ds' = \int_E^{E_0} Q_l(E')\frac{dE'}{S(E')}. \tag{5}$$

The stopping power $S(E) = -dE/ds$ is given by the average energy loss dE per path length ds. In the formulation of Joy and Luo [27], the energy loss dE in eV per unit path length ds in cm is

$$\frac{d\mathrm{E}}{ds} = -7.85\times10^{10}\frac{Z\rho}{AE}\ln\left(1.166\frac{E}{J'}\right), \tag{6}$$

with the mean ionization potential J' in eV given by

$$J' = \frac{1}{1+kJ/E}, \tag{7}$$

containing $k = 0.731 + 0.0688\times\log(Z)$ and $J = 9.76Z + 58.5Z^{-0.19}$ [28]. A is the atomic mass, Z the atomic number, and ρ the density of the material in g/cm^3.

The transport coefficients G_l have the dimension of an inverse length and are related to the inverse transport mean-free path: $\lambda_l^{-1} = G_l$ [29]. In particular, we have

$$\lambda_1^{-1} = \frac{2\pi}{\lambda}\int_{-1}^{1}(1-\cos\theta)f_1(\cos\theta)d(\cos\theta) = \frac{1-\langle\cos\theta\rangle}{\lambda}, \tag{8}$$

$$\lambda_2^{-1} = \frac{2\pi}{\lambda}\int_{-1}^{1}(1-\cos^2\theta)f_1(\cos\theta)d(\cos\theta) = \frac{1-\langle\cos^2\theta\rangle}{\lambda}. \tag{9}$$

The inverse of the first transport mean-free path λ_1^{-1} gives the average angular deflection per unit path length and is sometimes called the "scattering power," in analogy to the "stopping power," which is defined as mean energy loss per unit path length [29].

In this work, the extended versions of Lewis's first- and second-order moments are used in the formulation of Kawrakow and Bielajew [22] with the notation

$$k_l(s) = \exp\left[-\int_0^s Q_l(s')ds'\right] = \exp[-G_l(s)]. \tag{10}$$

The moments are given by

$$\langle\cos\theta\rangle = k_1(s) = \exp[-G_1(s)], \tag{11}$$

$$\langle z\rangle = \int_0^s k_1(s')ds', \tag{12}$$

$$\langle z^2\rangle = \frac{2}{3}\int_0^s ds'\int_0^{s'} k_1(s'-s'')[1+2k_2(s'')]ds'', \tag{13}$$

$$\langle x^2\rangle = \frac{2}{3}\int_0^s ds'\int_0^{s'} k_1(s'-s'')[1-k_2(s'')]ds'', \tag{14}$$

The mean deflection angle after multiple scattering events is given by its mean cosine $\langle\cos\theta\rangle$. The first moment $\langle z\rangle$ denotes the mean depth in the sample where the electron can be found after traveling a path length s. The second-order moments $\langle z^2\rangle$ and $\langle x^2\rangle$ give the mean squared longitudinal and lateral displacement of the electrons.

Considering energy loss for the calculation of the transport coefficients G_l determined by Eq. (5), the angular distribution of the electrons after $p = s/\lambda$ scattering events, i.e., their fraction N scattered per unit solid angle $d\Omega$, is given by [21]

$$F(\theta, s) = \frac{dN(\theta)}{d\Omega} = \sum_{l=0}^{\infty}\frac{2l+1}{4\pi}\exp(-G_l)\,P_l(\cos\theta). \tag{15}$$

This solution of the transport equation is exact but can be calculated only numerically. While the first- and second-order moments are determined by the first two transport coefficients G_1 and G_2, the summation in the angular distribution must be performed up to a high number of terms, typically several hundred [30]. Additionally, due to the expansion in fast oscillating Legendre polynomials, the difficulty to calculate the transport coefficients increases with their order and requires careful numerical techniques. We note that the application of this method is limited by the difficulty to solve the transport equation for electron scattering in inhomogeneous materials, which contain defects or interfaces between different materials.

In the following paragraph, we outline approximations of earlier approaches for the solution of the electron transport equation that were not made in the present work. Simpler analytical expressions for the moments and the angular distribution of the transport equation are obtained by assuming small-angle scattering and neglecting backscattering. In the small-angle approximation, the cosine of the scattering angle θ is expanded into a Taylor series:

$$\cos\theta \approx 1 - \frac{\theta^2}{2} + \cdots. \tag{16}$$

The Legendre polynomials and the transport coefficients in the small-angle approximation are given by [21]

$$P_l(\cos\theta) \approx 1 - \frac{l(l+1)}{4}\theta^2, \tag{17}$$

$$G_l = \frac{l(l+1)}{2}G_1. \tag{18}$$

Thus, the transport coefficients are completely determined by the value of the first transport coefficient G_1 [see Eq. (8)]:

$$G_1 = \frac{2\pi}{\lambda}\int_{-1}^{1}(1-\cos\theta)\,f_1(\cos\theta)d(\cos\theta), \tag{19}$$

with f_1 given by Eq. (4).

The angular distribution then simplifies to the Fokker-Planck formulation, as described by Wang and Guth [31]:

$$F_{FP}(\theta, s) = \sum_{l=0}^{\infty} \frac{2l+1}{4\pi} \exp\left[-\frac{l(l+1)}{2} G_1\right] P_l(\cos\theta). \quad (20)$$

While the first transport coefficient in the small-angle approximation is similar to the exact one, the approximated second transport coefficient is always $G_2 = 3G_1$ and for the moderate electron energies considered in this work larger than the exact value given by Eq. (5). Thus, the first-order moments, like the mean penetration depth $\langle z \rangle$, will not vary, but the second-order moments, i.e., the variances of the longitudinal and lateral displacements $\langle z^2 \rangle$ and $\langle x^2 \rangle$ will change. Also, the angular distribution will provide lower values than the exact solution, due to the general larger values of the transport coefficients G_l in the small-angle approximation.

In the small-angle approximation, the Fokker-Planck formulation simplifies and leads to a Gaussian solution [21]. Thus, neglecting large-angle scattering and energy loss, the Gaussian angular distribution of the scattered electrons is [17]

$$F_G(\theta, s) = \frac{1}{2\pi\theta_m^2} \exp\left(-\frac{\theta^2}{2\theta_m^2}\right), \quad (21)$$

where the mean-square scattering angle θ_m^2 can be approximated by

$$\theta_m^2 = 1.2 \times 10^7 \frac{Z^{1.5}}{AE} \rho s, \quad (22)$$

with the atomic number Z, the atomic mass A in atomic mass units, the electron energy E in eV, and the mass density ρs in g/cm^2. The angular distribution in this analytical Gaussian formulation does not need any numerical computation and can be plotted directly as a function of the scattering angle.

The drawbacks of the models, which assume small-angle scattering, led to Lewis's intention to formulate the solution of the transport equation without these limitations [21].

B. Analytical models for beam broadening

Several analytical approaches for electron-beam broadening in matter were proposed. Usually, they neglect large-angle scattering and energy loss. This means that the models are limited to electron-transparent samples in STEM where the majority of the electrons are scattered in forward direction. Reimer calculated the beam broadening by giving the root mean square of the variance of the lateral displacement [18]. By assuming a Gaussian scattering distribution and integrating over the sample thickness *t,* he obtained

$$r_{\mathrm{rms}} = \sqrt{2} \times 1.05 \times 10^5 \frac{Z}{E_0} \left(\frac{\rho}{A}\right)^{0.5} t^{1.5}, \quad (23)$$

with the beam radius r_{rms} and the thickness t in cm, the primary electron energy E_0 in eV, the material density ρ in g/cm^3, the atomic number Z, and the atomic mass A in g/mol.

Goldstein *et al.* assumed electron scattering in the middle of a foil with thickness t and integrated the unscreened Rutherford differential scattering cross section up to a defined scattering angle, which defines the width of the beam b [15]. They found for the beam width at the exit surface of the sample:

$$b = a \frac{Z}{E_0} \left(\frac{\rho}{A}\right)^{0.5} t^{1.5}, \quad (24)$$

with the sample thickness t and beam broadening b in units of nm and E_0 in keV. The factor a depends on the fraction of beam intensity considered for the definition of the beam diameter. For a beam diameter containing 68% of the total beam intensity, corresponding to the variance of a Gaussian distribution, the constant is $a = 0.11$ nm keV. Assuming constant probability for electron scattering at each sample depth and integrating over the sample thickness leads to a slightly modified factor $a = 0.13$ nm keV [16].

A more sophisticated model was proposed by Gauvin and Rudinsky, valid for a large range of the number of elastic collisions $p = t/\Lambda_{\mathrm{el}}$ with the mean-free path length for elastic scattering Λ_{el} [10]. They calculated the width of the beam at a thickness t by

$$b = K' \frac{Z^{(4H+1)/3}}{E_0^{(2H+1)/2}} \left(\frac{\rho}{A}\right)^{H} t^{1+H}, \quad (25)$$

with

$$K' = 0.1167^{1-2H}\ 39437^{H} \sqrt{\frac{R}{1-R}}, \quad (26)$$

where the Hurst exponent H is characteristic for different scattering regimes depending on the number of collisions p. R denotes the fraction of the total electron beam intensity that defines the beam diameter. In this work, it is set to $R = 0.68$. The constants in Eq. (25) are calculated to yield beam broadening in units of cm with the material density ρ in g/cm^3 and E_0 in units of keV. The Hurst exponent approaches 1 for small sample thicknesses with $p \to 0$ in the ballistic regime where electrons may not be scattered at all. For plural and multiple scattering, the electrons reach random walk behavior which is characterized by $H = 0.5$. In this case, Eq. (25) reduces to Eq. (24) but with a different factor a.

C. Numerical solution of the electron transport equation

The solution of the electron transport equation is implemented numerically to calculate the angular distribution for multiple scattering, similar to the approach of Negreanu *et al.* [30]. It is extended by routines for computation of the moments of the spatial electron distribution. For this purpose, we developed the software package CeTE (Computation of electron Transport Equation). The code is written in Java (Java Software, Oracle) and can be executed on any common personal computer.

First, the mean range of electrons, where their residual energy goes to zero, is determined by the continuous-slowing-down approximation of Joy and Luo depending on the primary electron energy [27]. Up to this mean range, energy loss is calculated for path steps $ds = 10$ nm and the residual energies of the electron after traveling γ steps corresponding to the path $s = \gamma ds$ are stored in an array. To account for energy straggling determined by the distribution of the path lengths around their mean value, the list of the residual energy values

is convoluted with a Poisson function, as proposed by Reimer and Senkel [32]. Then the residual energy at the position γ in a new array is

$$E(\gamma) = \sum_{n=0}^{3\gamma} P(n,\gamma)E(n), \tag{27}$$

with the Poisson distribution

$$P(n,\gamma) = \frac{\gamma^n}{n!}e^{-\gamma}. \tag{28}$$

The summation over n is performed from 0 to 3γ, where the Poisson distribution with the variance $\sqrt{\gamma}$ gives negligible values. For values of $n > 30$ the Poisson distribution is calculated by a Gaussian approximation with $\sigma^2 = \gamma$. A new array for the residual energy as a function of the traveled path is obtained, with an extended range, where the residual energy vanishes. This new maximum range of the electrons in the corresponding material determines the traveled distance where all electrons are absorbed.

The transport coefficients $G_l(E_i)$ are calculated in steps of 1 keV for E_i up to the primary electron energy E_0 and are interpolated linearly for intermediate values. An N-point Gauss-Legendre quadrature formula is used to evaluate the integral in Eq. (5) and Eq. (3), as described by Negreanu *et al.* [30].

The Legendre polynomials are calculated by their recurrence relations:

$$P_0(x) = 1, \quad P_1(x) = x,$$
$$P_l(x) = \frac{1}{l}\left[(2l-1)xP_{l-1}(x) - (l-1)P_{l-2}(x)\right]. \tag{29}$$

The maximum number N_l of Legendre coefficients is selected in advance and determines the upper limit of the summation in Eq. (2). For low electron energies and typically short mean-free path lengths in solids, $N_l = 500$ is sufficient for the convergence of the series. This number also determines the number of intervals N in the N-point quadrature formula [30]. The moments given by Eqs. (11)–(14) are obtained by evaluating the integrals as Riemann sums, in steps of 1 nm. For each step, the energy loss is calculated and the corresponding transport coefficients $G_l(E_i)$ are summed up, yielding the coefficients given by Eq. (5). The moments $\langle z^2\rangle$ and $\langle x^2\rangle$ determine the interaction volume and the beam radius at the mean depth $\langle z\rangle$. For calculation of energy deposition in matter, the traveled path length s and the reached depth $\langle z\rangle$ are used.

Subsequently, the angular scattering distribution is obtained for each sample thickness and primary electron energy according to Eq. (15). Separating the contribution of the unscattered electrons from the summation, the convergence of the serial expansion is improved by writing [30]

$$F(\theta,s) = \exp\left(-\frac{s}{\lambda}\right)\frac{\delta(\cos\theta-1)}{\pi} + \sum_{l=0}^{N_l}\frac{2l+1}{4\pi}\left[\exp(-G_l) - \exp\left(-\frac{s}{\lambda}\right)\right]P_l(\cos\theta), \tag{30}$$

where $\delta(\cos\theta - 1)$ is the Dirac delta function. Various differential screened Rutherford scattering cross sections and the Mott cross sections tabulated by Czyzeweski *et al.* (1990) were implemented in the code and can be selected accordingly. The contribution of inelastic scattering to the angular distribution is considered by multiplying the screened Rutherford cross sections by $(1 + 1/Z)$, where Z is the average atomic number of the material [18].

The transport coefficients G_l from Eq. (5) are generally calculated in this work as a function of the energy loss determined by the continuous-slowing-down approximation. Only for comparison with the analytical models, which neglect energy loss, the G_l are calculated for constant electron energy along the path.

The angular distribution of electrons after traveling a path length s according to Eq. (30) is determined in this work typically for angular step sizes of 0.01 rad, but can be varied accordingly, if necessary.

For comparison, the Fokker-Planck small-angle approximation Eqs. (16)–(20) is also implemented in the code.

D. Comparison of calculated beam broadening from different models

We first compare calculated beam radii from the models of Reimer, Goldstein, and Gauvin [cf. Eqs. (23)–(25)]. In Sec. III these models will be compared to solutions of the electron transport equation. For this, the beam diameter is defined as the radius of the volume containing 68% of the electrons of the primary beam after traveling a path length s. The constants in the Goldstein and Gauvin models are adapted accordingly [cf. Eqs. (24) and (25)]. In Reimer's model, the beam diameter is already defined as the variance of the Gaussian distribution, which comprises 68% of the primary electrons. As a measure for the beam broadening, Reimer's approach gives the radius of the beam while propagating into the sample whereas the other analytical models describe the total width of the beam by its diameter b, which is twice the radius. Therefore, we compare the beam radius $r_{\rm rms}$ of Reimer's Eq. (23) with $b/2$ of the other models expressed by Eqs. (24) and (25).

Figure 1 shows calculated beam radii obtained by applying the models of Reimer, Goldstein, and Gauvin according to Eqs. (23)–(25) as a function of the sample thickness for silicon with $Z = 14$, $A = 28.09$, and $\rho = 2.33\,\mathrm{g/cm^2}$ and electron energies between 10 keV and 30 keV. For the Gauvin model, we assumed $H = 0.5$ corresponding to plural and multiple scattering. For these scattering regimes that are relevant for the considerations of this work, the Reimer and Gauvin approaches give almost identical results. Therefore, we will only consider the data obtained by the Reimer and Goldstein models in the following. In general, the Goldstein model yields a slightly stronger beam broadening than the Reimer model.

The analytical models considered here do not take into account energy loss and large-angle scattering. The small-angle approximation implies that the path length traveled between two consecutive deflections is equal to its projection onto the z axis. This assumption is not generally valid, which will be illustrated in Fig. 2. For this purpose, we present results for beam broadening using the solution of the transport equation outlined in Secs. II A and II C. Here, the variances of the

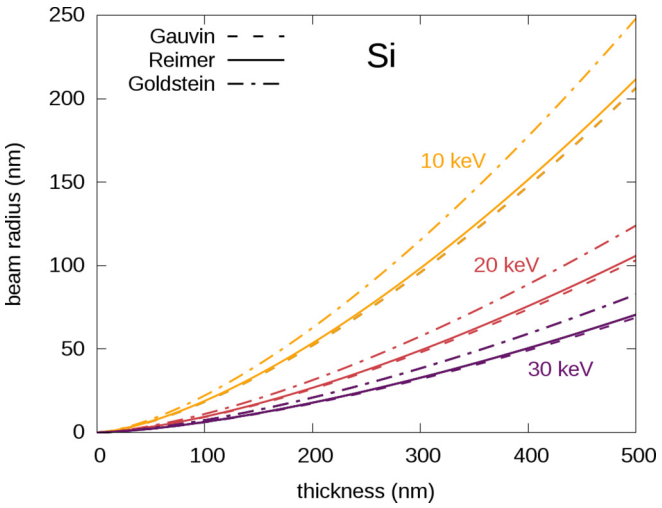

FIG. 1. Beam radii in silicon as a function of sample thickness calculated by the indicated analytical models for different primary electron energies. Energy loss and large-angle scattering are neglected.

longitudinal and lateral displacement $\langle z^2 \rangle$ and $\langle x^2 \rangle$ are calculated from Eqs. (13) and (14). The root mean squares of the displacements $\sigma_z = \sqrt{\langle z^2 \rangle - \langle z \rangle^2}$ and $\sigma_x = \sigma_y = \sqrt{\langle x^2 \rangle}$ determine the region where the electron is less than one standard deviation away from the mean displacement. These zones are shown in Fig. 2 for the example of silicon and 20 keV electrons for different traveled path lengths $s = 300$, 600, and 900 nm as ellipses with the center at the mean penetration depth $\langle z \rangle$ and with the major axis given by σ_x and the minor axis by σ_z.

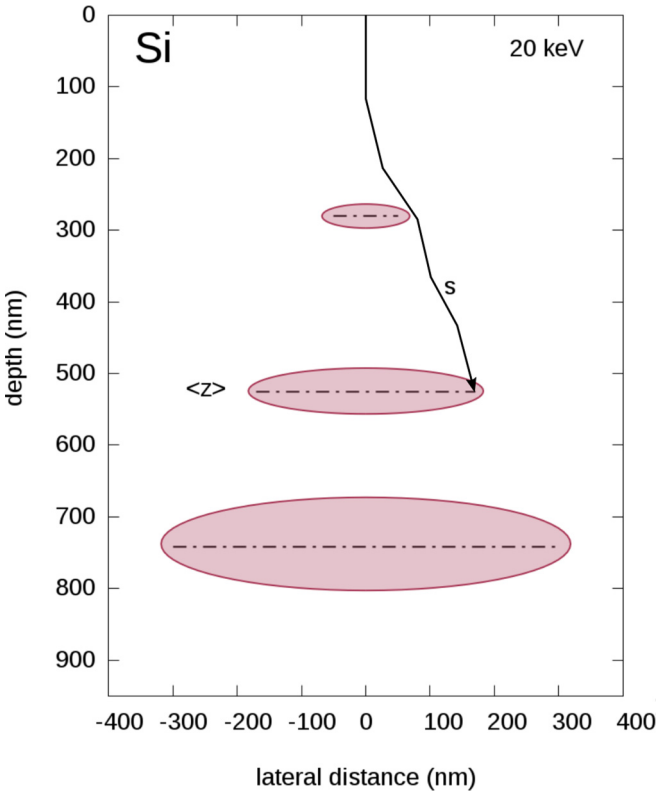

FIG. 2. Spatial distribution of 20 keV electrons after traveling different path lengths s in silicon. Ellipses centered at the mean penetration depth $\langle z \rangle$ (indicated by dashed-dotted horizontal lines) for s = 300, 600, and 900 nm show the distribution of the electrons less than one standard deviation away from the mean displacement.

We note that the beam radius $r = \sqrt{x^2 + y^2}$ at the depth $\langle z \rangle$ calculated by solving the electron transport equation is given by the root mean square of a lateral displacement:

$$\sigma_r = \sqrt{\left(\frac{\partial r}{\partial x}\sigma_x\right)^2 + \left(\frac{\partial r}{\partial y}\sigma_y\right)^2} = \sigma_x = \sigma_y. \tag{31}$$

For Poisson-distributed paths, which become Gaussian-like for plural and multiple scattering, 68% of the electrons are within a spheroid with the radius r.

Figure 2 also illustrates that the electron reaches a depth $\langle z \rangle$ below the sample surface, related to the sample thickness, which differs from the traveled path length s. For example, the dash-dotted line in the ellipse in the center of the image indicates $\langle z \rangle = 520$ nm, which is considerably smaller than $s = 600$ nm in this case. The discrepancies between $\langle z \rangle$ and s increase with increasing path length as shown by the ellipses in Fig. 2.

In the following, the results of this work are illustrated by calculations for silicon with low atomic number and moderate material density, for copper with higher atomic number $Z = 29$, atomic mass $A = 63.54$ and material density $\rho = 8.96\,\mathrm{g/cm^2}$, and for the strongly scattering platinum with $Z = 78$, $A = 195.08$, and $\rho = 21.45\,\mathrm{g/cm^2}$, representing main parameters for electron scattering in matter. The thickness ranges are chosen with regard to the primary electron energies so that all main scattering regimes are covered, i.e., single, plural, and multiple scattering and at least for some cases diffusion and absorption. The diffusion regime is characterized by isotropic scattering of the electrons, while absorption occurs when the electron has completely lost its energy and its maximum range is reached.

III. RESULTS AND DISCUSSION

A. Mean penetration depth and mean scattering angles

Solving the transport equation and calculating the first moments $\langle z \rangle$ and $\langle \cos\theta \rangle$ of the spatial distribution shows that the electrons are scattered away from the initial direction defined as the z axis of the coordinate system. The mean penetration depth $\langle z \rangle$, i.e., the average distance of all electrons from the surface of the sample, is smaller than the path length s as shown for silicon in Fig. 3(a). The depth corresponding to a value equal to the path length is indicated by a dashed line, while values for the mean penetration depth for different primary energies are plotted by colored lines. The difference between reached depth and overall traveled path increases with the number of scattering events, which is higher for lower primary electron energies and increasing path lengths. The mean penetration depth approaches a constant value, as it can be seen best for 10 keV electrons. Here the diffusion regime is reached already at comparably small s values, where the electrons are scattered isotropically and continue traveling in

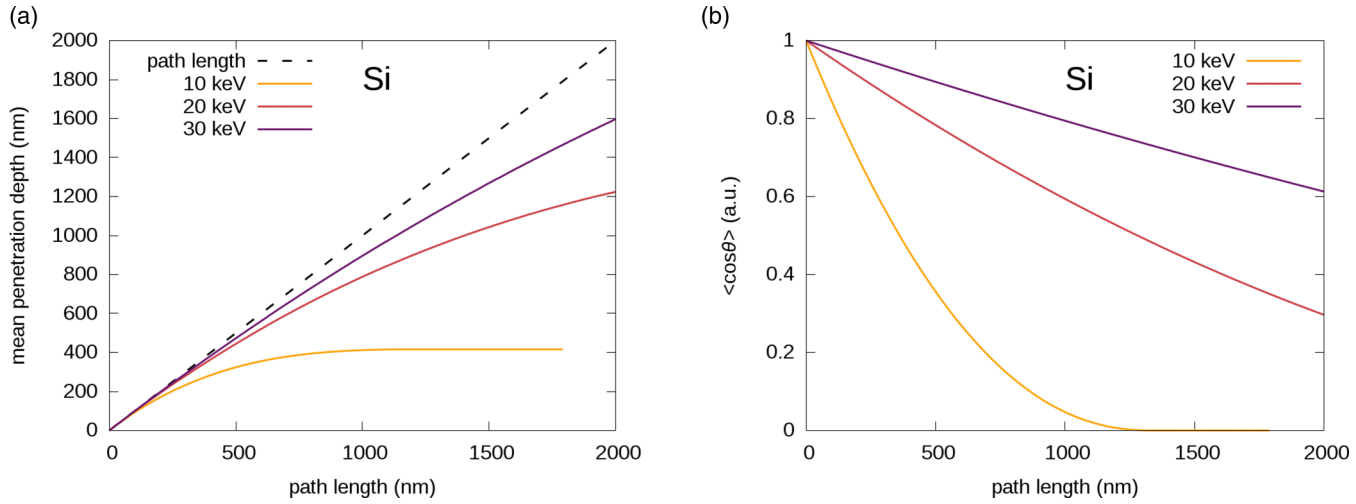

FIG. 3. (a) Mean penetration depth in silicon for electrons of different primary energies as a function of the traveled path length. The dashed-dotted line indicates a depth equal to the path length. (b) Mean cosine of the scattering angle as a function of the traveled path length in silicon for electrons of different primary energies.

all directions, but in average their penetration depth $\langle z \rangle$ below the surface remains constant.

The difference between s and $\langle z \rangle$, the so-called path length correction, must be taken into account when analyzing the propagation of the electrons in the initial incidence direction. The traveled path determines the number of elastic and inelastic collisions and affects explicitly the spatial, angular, and energy distribution. The reached depth is the projected path in the direction of increasing sample thickness. The mechanism of beam broadening is usually described by a function of the sample thickness, i.e., at depths below the surface, but must be calculated in terms of effective traveled path lengths.

The mean cosine of the scattering angle $\langle \cos\theta \rangle$ is a measure for the spreading of the initial small-diameter electron beam due to multiple scattering. For a strongly forward peaked beam, $\langle \cos\theta \rangle$ is close to unity and its value approaches zero if the diffusion regime is reached. Figure 3(b) shows $\langle \cos\theta \rangle$ for electrons of different energies as a function of the traveled path length in silicon. With decreasing initial electron energy, $\langle \cos\theta \rangle$ drops faster and approaches zero for the diffusion regime. The 10 keV curve in Fig. 3(a) shows that a constant value of the mean penetration depth is reached for a path length of approximately 700 nm. A small value of 0.2 for the mean cosine of the scattering angle is found for $s = 700$ nm in Fig. 3(b), indicating a diffusion-like scattering regime. For the diffusion regime the angular distribution of the electrons from Eq. (15) becomes an isotropic distribution with $F(\theta, s) = 1/(4\pi)$.

B. Beam broadening and comparison with analytical models

The electron beam radius r at the mean penetration depth $\langle z \rangle$ obtained in this work by the method of moments (MM) is compared with the calculations of Reimer and Goldstein [15,18]. As outlined before, it was assumed for the calculation with the analytical equations that the thickness t, i.e., $\langle z \rangle$, corresponds to the traveled path length s. The results of Gauvin's model are not shown here because they essentially agree with Reimer's model (see Fig. 1).

Figure 4(a) shows the beam radius as a function of $\langle z \rangle$ in silicon for different primary electron energies. For comparison and discussion reasons, only for this figure, the moments were calculated with the small-angle approximation and energy loss was neglected along the electron path, corresponding to the assumptions of the two analytical models. The curves show similar behavior with beam broadening $b \sim t^{1.5}$ up to a relatively large penetration depth. Then the beam radius calculated by MM increases more pronounced than those of the analytical methods, which is observed for the 10 keV curve at penetration depths beyond 500 nm. Obviously, the analytical models do not consider that the electrons approach the diffusion regime, where the scattering becomes isotopic, and the mean penetration depth approaches a final constant value for all electrons on average. This becomes clearer in Fig. 4(b) where the moments were calculated without restriction to small scattering angles and the energy loss was also taken into account, whereas the analytical curves still contain the approximation for small-angle scattering and neglect energy loss. For 10 keV electrons, the final mean penetration depth from MM is reached already at about 400 nm. Although most electrons can be found on average at this depth limit, they still move, spreading laterally to r = 600 nm until their energy is zero (indicated by the termination of the yellow line), where the traveled path reaches the total range. With increasing primary energy, the maximum mean penetration depth increases, and the diffusion range is reached at larger depth

Similarly, Fig. 4(c) shows the radius of the electron beam in copper as a function of the penetration depth. For 10 keV electrons, the beam width increases up to 180 nm until the total traveled path s approaches the maximum range and the electrons are absorbed. The diffusion regime is reached already at a depth of about 70 nm. Platinum was considered as an example for a strongly scattering material [Fig. 4(d)] where the diffusion regime commences already at 17 nm depth for 10 keV and at 120 nm for 30 keV. We conclude from the results in Fig. 4 that beam broadening calculated by the MM and the analytical models is in very good agreement up to the penetration depth where the diffusion regime is reached.

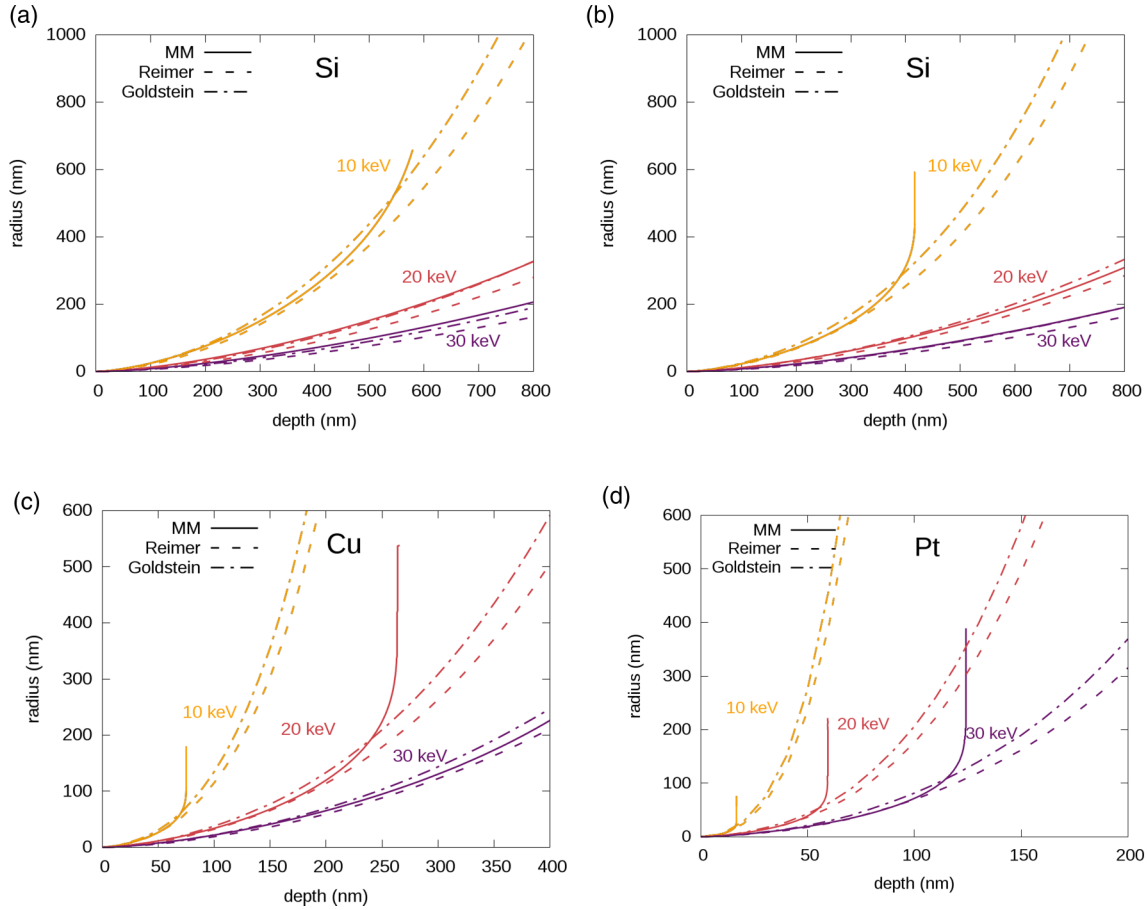

FIG. 4. Beam radius as a function of penetration depth $\langle z \rangle$ for the Reimer (dashed), Goldstein (dashed-dotted), and MM (continuous lines) formalisms for primary electron energies of 10, 20, and 30 keV indicated by different colors. (a) Beam radius in Si for the small scattering-angle approximation and neglecting energy loss. (b)–(d) Beam radius in Si, Cu, and Pt, respectively, taking into account energy loss along the electron path and without limitation to small scattering angles for the MM.

Figures 5(a) and 5(b) show the spatial displacement of 10 and 30 keV electrons in copper with increasing $\langle z \rangle$. Ellipses with centers at different mean penetration depth $\langle z \rangle$ and the semiaxes σ_r and σ_z in lateral and depth directions, respectively, indicate a 68% probability to find the electron in this zone. This corresponds to 68% of the interaction volume at a certain $\langle z \rangle$. The increasing size of the interaction volume shows electron propagation up to a final extension, where the electrons approach their total range. The interaction volume is larger at higher primary electron energies, as shown in Fig. 5(b) for 30 keV in comparison to 10 keV in Fig. 5(a). We emphasize that the total traveled path is always larger or

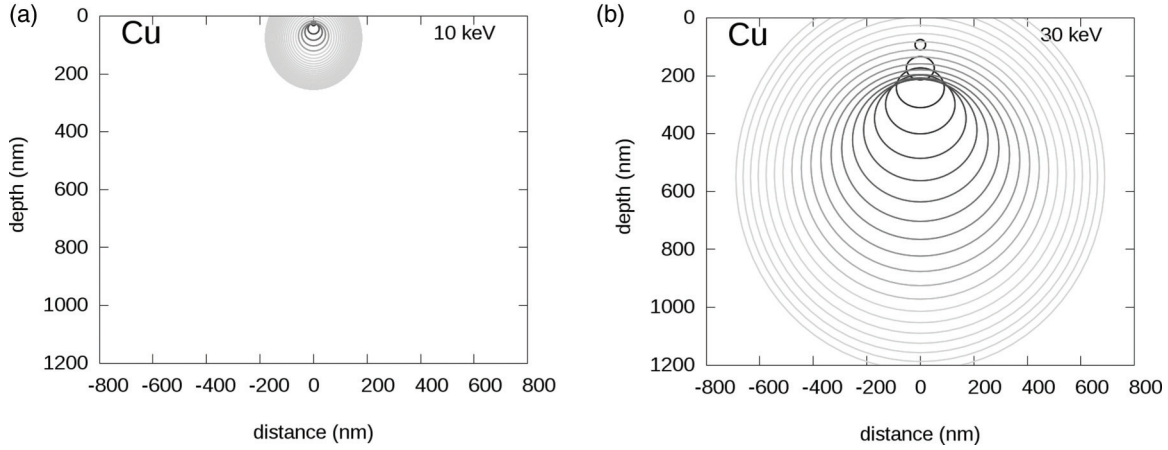

FIG. 5. Time evolution of beam spreading in Cu for (a) 10 keV and (b) 30 keV. The ellipses drawn with centers at different mean penetration depths contain 68% of the scattered electrons.

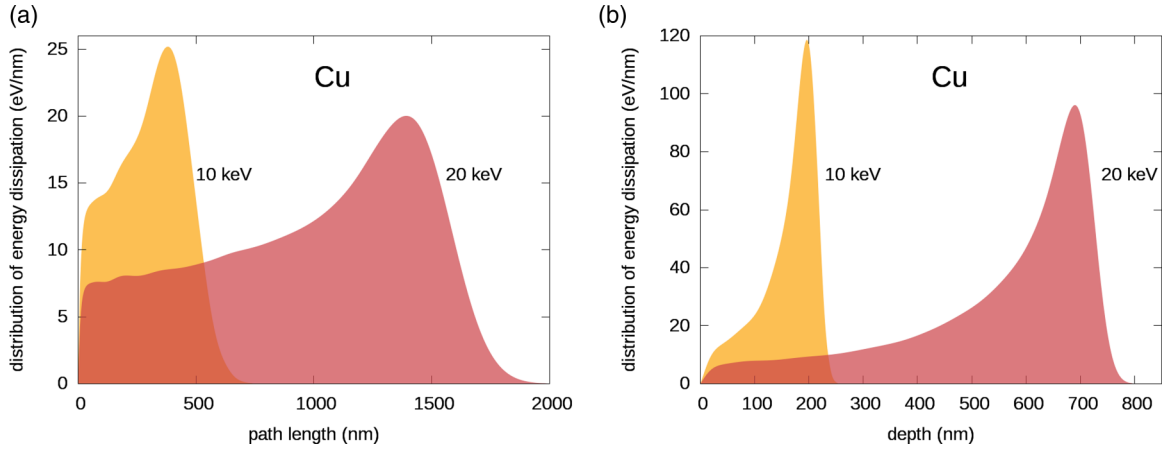

FIG. 6. Energy dissipation in copper as a function of (a) traveled path length s and (b) depth $\langle z\rangle + \sigma_z$ below the sample surface for primary electron energies of 10 and 20 keV.

equal to the sum of r and $\langle z\rangle$. Moreover, the ellipses do not correspond to the angular distribution of the electrons, which is isotropic only when the diffusion regime is reached.

C. Energy dissipation in matter

The residual energy of the electrons after traveling a distinct path was calculated numerically and by taking into account Poisson-distributed straggling as previously described. The gradient of the residual energy with respect to s provides the energy loss per unit path length $dE(s)/ds$ corresponding to the distribution of the dissipated energy. Figure 6(a) shows the energy per step of path length ds deposited in copper for 10 and 20 keV electrons. The energy dissipation increases to a maximum at a certain path length, depending on the material properties and the primary electron energy following Eq. (6). Beyond this maximum, the dissipated energy decreases strongly towards a smooth tail due to the Gaussian-like distribution of the path lengths at the range limit. The path length, where the energy dissipation is zero, represents the maximum range, where all electrons are absorbed. As shown in Fig. 3(a), the difference between traveled path length and mean reached depth increases with the number of collisions. Also, the step ds differs from the thickness step dt and therefore $dE(s)/ds$ does not represent the energy deposited in equidistant layers of thickness below the surface. The more informative deposited energy $dE(t)/dt$ in steps of depth dt below the surface is given with the notation of this work by the energy loss as a function of steps of penetration depths $d\langle z\rangle$. Plotting the energy dissipation only as a function of $\langle z\rangle$, without taking into account its variance, would give rise to a meaningless peak close to the diffusion regime due to the constant value of the mean penetration depth and the singularity of the derivative at $dt = 0$. Therefore, the distribution of the energy dissipation is plotted in Fig. 6(b) as a function of the sum of mean penetration depth $\langle z\rangle$ and its standard deviation $\sqrt{\langle z^2\rangle - \langle z\rangle^2}$, i.e., $dE(t')/d(t')$ where $t' = \langle z\rangle + \sigma_z$. The depth reached in the sample is lower than the path length s and therefore the energy dissipation curve is more compressed than in Fig. 6(a), while its maximum is much sharper. On the other hand, the deposited energy per unit volume, obtained by dividing the dissipated energy by the cross section of the beam πr^2, decreases continuously due to the increasing radius of the electron beam.

D. Angular distribution of multiple-scattered electrons and comparison with approximating models

The ellipses in Fig. 5. indicate the interaction volume and the position of 68% of the electrons after traveling a distinct path. The electrons are isotropically distributed in these regions only in the diffusion case. In general, before the diffusion regime is reached, the direction of motion of the scattered electrons is given by the angular distribution $F(\theta, s)$ determined by Eq. (30) from the transport equation, or by the approximations mentioned before [Eq. (20) and (21)]. $F(\theta, s)$ is shown in Fig. 7 for 20 keV electrons in silicon. Results calculated by CeTE are plotted with a continuous black line, while the data obtained by Cosslett's Gauss and the Fokker-Planck approximations are shown by a dotted and a dashed line respectively. Figure 7(a) shows the results after a path length $s = 300$ nm in silicon. For small scattering angles, both the Fokker-Planck and the Gaussian approximations yield substantially lower values than the exact (CeTE) ones. Figure 7(b) shows the angular distribution after traveling a path length $s = 500$ nm in silicon. Forward scattering decreases with larger traveled path lengths, and more electrons are scattered into higher angles. The Fokker-Planck approximation shows the same behavior as before, yielding lower values at smaller angles and slightly higher ones than the exact solution at higher scattering angles. The Gauss approximation is close to the exact solution, suggesting that this approximation is valid for materials with sufficiently high material thicknesses and moderate primary electron energies. However, at higher thicknesses the Gaussian angular distribution deviates from the distribution calculated by CeTE because it shows more pronounced forward-scattering, as illustrated in Fig. 7(c).

Knowing the distribution of the emitted electrons helps to interpret the intensities measured by different detectors since those collect electrons usually within a defined angular range. This corresponds to an integration of the curves in Fig. 7 over $d\Omega$ for defined limits of the scattering angle θ.

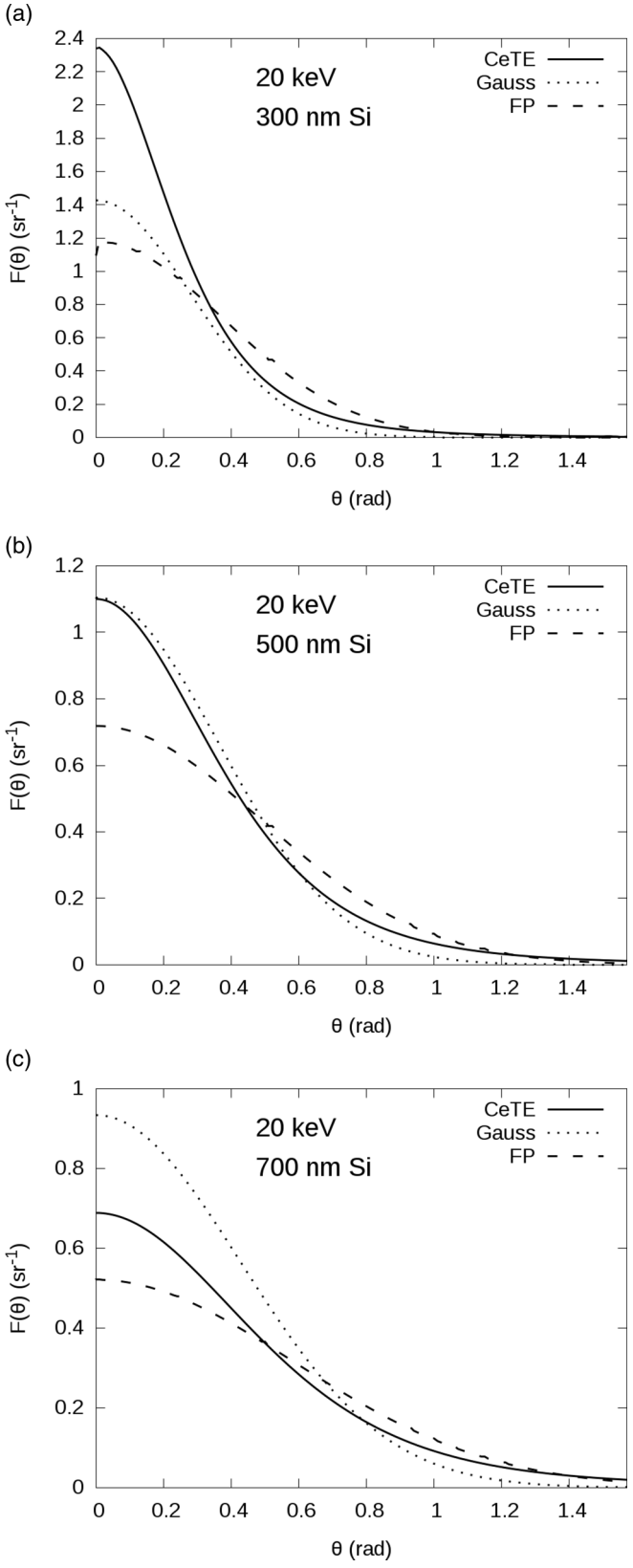

FIG. 7. Angular distribution of 20 keV electrons after traveling a path length s of (a) 300 nm, (b) 500 nm, and (c) 700 nm in silicon obtained by the exact solution of the transport equation (continuous line), Cosslett's Gaussian distribution (dotted line), and the solution with the Fokker-Planck approximation (dashed line).

IV. CONCLUSIONS

The interaction of a focused electron beam impinging on a solid is described in this work in a general way by solving the electron transport equation in the formulation of Lewis [21]. The numerical calculations were performed similar to the approach of Negreanu *et al.* [30], but in this work we have taken into account energy loss by the continuous-slowing-down approximation [27]. Exact solutions for all scattering regimes (single scattering and multiple scattering) are obtained without approximations such as dominant forward scattering and negligible energy loss. The extended versions of Lewis's first- and second-order moments in the formulation of Kawrakow and Bielajew [22] were calculated in this work to determine electron-beam broadening, the size of the interaction volume, and the energy dissipation of the electrons for bulk and electron-transparent samples. The results are not limited to electrons energies between 10 and 30 keV, which are typical for scanning electron microscopes, but apply also to higher electron energies used in transmission electron microscopes as long as the contribution of coherence effects can be neglected.

The results obtained in this work differ significantly from other models which are based on simplifications like forward scattering and negligence of energy loss. One important finding is that the mean penetration depth of the electrons, corresponding to the sample thickness t, is always smaller than the traveled path length s. The difference between s and t increases with the sample thickness. Beam broadening, energy dissipation, and interaction volumes are typically analyzed in terms of t, which approaches a constant value although s and the lateral displacement of the electrons still increase until the maximum range is reached. The calculated energy dissipation dE/ds has to be transformed into dE/dt, resulting in energy loss at smaller sample thicknesses as predicted by analytical models.

The first- and second-order moments obtained from the spatial electron distribution can be used for the calculation of the size of the interaction volume of the scattered electrons within the material. This corresponds to the volume containing 68% of the electrons after traveling a distinct path length s. The direction of motion of the electrons in the interaction volume is obtained by their angular distribution.

This work will allow a more differentiated view on resolution, which depends not only on the instrumental properties but also on the analyzed sample as well.

ACKNOWLEDGMENTS

The authors acknowledge funding by the Deutsche Forschungsgemeinschaft (DFG, German Research Foundation) under Germany's Excellence Strategy via the Excellence Cluster 3D Matter Made to Order (EXC-2082/1 – 390761711). We also thank the Carl Zeiss Foundation for financial support and acknowledge support by the KIT-Publication Fund of the Karlsruhe Institute of Technology.

D.G. supervised the project. E.M. conceived the project, performed the calculations, and wrote the main part of the paper, with contributions from all other authors. M.H. contributed to the discussion of the methods. All authors read the manuscript and contributed to the discussion of the results.

[1] P. E. Batson, N. Dellby, and O. L. Krivanek, Sub-ångstrom resolution using aberration corrected electron optics, Nature (London) **418**, 617 (2002).

[2] N. Shibata, S. J. Pennycook, T. R. Gosnell, G. S. Painter, W. A. Shelton, and P. F. Becher, Observation of rare-earth segregation in silicon nitride ceramics at subnanometre dimensions, Nature (London) **428**, 730 (2004).

[3] Y. Sun, L. Zhao, H. Pan, X. Lu, L. Gu, Y.-S. Hu, H. Li, M. Armand, Y. Ikuhara, L. Chen *et al.*, Direct atomic-scale confirmation of three-phase storage mechanism in $Li_4Ti_5O_{12}$ anodes for room-temperature sodium-ion batteries, Nat. Commun. **4**, 1870 (2013).

[4] P. Gao, S. Yang, R. Ishikawa, N. Li, B. Feng, A. Kumamoto, N. Shibata, P. Yu, and Y. Ikuhara, Atomic-Scale Measurement of Flexoelectric Polarization at $SrTiO_3$ Dislocations, Phys. Rev. Lett. **120**, 267601 (2018).

[5] M. Haider, S. Uhlemann, E. Schwan, H. Rose, B. Kabius, and K. Urban, Electron microscopy image enhanced, Nature (London) **392**, 768 (1998).

[6] O. L. Krivanek, N. Dellby, and A. R. Lupini, Towards sub-Å electron beams, Ultramicroscopy **78**, 1 (1999).

[7] C. Kisielowski, B. Freitag, M. Bischoff, H. van Lin, S. Lazar, G. Knippels, P. Tiemeijer, M. van der Stam, S. von Harrach, M. Stekelenburg *et al.*, Detection of single atoms and buried defects in three dimensions by aberration-corrected electron microscope with 0.5-Å information limit, Microsc. Microanal. **14**, 469 (2008).

[8] O. L. Krivanek, M. F. Chisholm, V. Nicolosi, T. J. Pennycook, G. J. Corbin, N. Dellby, M. F. Murfitt, C. S. Own, Z. S. Szilagyi, M. P. Oxley *et al.*, Atom-by-atom structural and chemical analysis by annular dark-field electron microscopy, Nature (London) **464**, 571 (2010).

[9] U. Kaiser, J. Biskupek, J. C. Meyer, J. Leschner, L. Lechner, H. Rose, M. Stöger-Pollach, A. N. Khlobystov, P. Hartel, H. Müller *et al.*, Transmission electron microscopy at 20 kV for imaging and spectroscopy, Ultramicroscopy **111**, 1239 (2011).

[10] R. Gauvin and S. Rudinsky, A universal equation for computing the beam broadening of incident electrons in thin films, Ultramicroscopy **167**, 21 (2016).

[11] H. Drees, E. Müller, M. Dries, and D. Gerthsen, Electron-beam broadening in amorphous carbon films in low-energy scanning transmission electron microscopy, Ultramicroscopy **185**, 65 (2017).

[12] M. Hugenschmidt, E. Müller, and D. Gerthsen, Electron beam broadening in electron-transparent samples at low electron energies, J. Microsc. **274**, 150 (2019).

[13] N. de Jonge, A. Verch, and H. Demers, The influence of beam broadening on the spatial resolution of annular dark field scanning transmission electron microscopy, Microsc. Microanal. **24**, 8 (2018).

[14] M. Hatzakis, New method of observing electron penetration profiles in solids, Appl. Phys. Lett. **18**, 7 (1971).

[15] J. I. Goldstein, J. L. Costley, G. W. Lorimer, and S. J. B. Reed, Quantitative x-ray analysis in the electron microscope, Scanning Electron Microscopy **1**, 315 (1977).

[16] S. J. B. Reed, The single-scattering model and spatial resolution in x-ray analysis of thin foils, Ultramicroscopy **7**, 405 (1982).

[17] V. E. Cosslett and R. N. Thomas, Multiple scattering of 5–30 keV electrons in evaporated metal films. I. Total transmission and angular distribution, Br. J. Appl. Phys. **15**, 883 (1964).

[18] L. Reimer, *Scanning Electron Microscopy, Physics of Image Formation and Microanalysis* (Springer, Heidelberg, 1998), Vol. 45.

[19] D. C. Joy, *Monte Carlo Modeling for Electron Microscopy and Microanalysis*, Oxford Series in Optical and Imaging Science Vol. 9 (Oxford University Press, New York, 1995).

[20] S. Goudsmit and J. L. Saunderson, Multiple scattering of electrons, Phys. Rev. **57**, 24 (1940).

[21] H. W. Lewis, Multiple scattering in an infinite medium, Phys. Rev. **78**, 526 (1950).

[22] I. Kawrakow and A. F. Bielajew, On the condensed history technique for electron transport, Nucl. Instrum. Methods Phys. Res. B **142**, 253 (1998).

[23] P. Rez, A transport equation theory of beam spreading in the electron microscope, Ultramicroscopy **12**, 29 (1983).

[24] P. M. Voyles, D. A. Muller, and E. J. Kirkland, Depth-dependent imaging of individual dopant atoms in silicon, Microsc. Microanal. **10**, 291 (2004).

[25] R. J. Wu, A. Mittal, M. L. Odlyzko, and K. A. Mkhoyan, Simplifying electron beam channeling in scanning transmission electron microscopy (STEM), Microsc. Microanal. **23**, 794 (2017).

[26] E. W. Larsen, M. M. Miften, B. A. Fraass, and I. A. Bruinvis, Electron dose calculations using the Method of Moments, Med. Phys. **24**, 111 (1997).

[27] D. C. Joy and S. Luo, An empirical stopping power relationship for low-energy electrons, Scanning **11**, 176 (1989).

[28] J. I. Goldstein, D. E. Newbury, J. R. Michael, N. W. M. Ritchie, J. H. J. Scott, and D. C. Joy, *Scanning Electron Microscopy and X-Ray Microanalysis* (Springer, New York, 2018).

[29] J. M. Fernández-Varea, R. Mayol, J. Baró, and F. Salvat, On the theory and simulation of multiple elastic scattering of electrons, Nucl. Instrum. Methods Phys. Res. B **73**, 447 (1993).

[30] C. Negreanu, X. Llovet, R. Chawla, and F. Salvat, Calculation of multiple-scattering angular distributions of electrons and positrons, Radiat. Phys. Chem. **74**, 264 (2005).

[31] M. C. Wang and E. Guth, On the theory of multiple scattering, particularly of charged particles, Phys. Rev. **84**, 1092 (1951).

[32] L. Reimer and R. Senkel, Calculation of energy spectra of electrons transmitted through thin aluminium foils, J. Phys. D **25**, 1371 (1992).